东南大学图书馆
Southeast University Library

东图学术快报
Academic express of SEU LIB

前沿经典　学科热点

学术动态　工具助手

编者按：2021 年不仅是“十四五”的开局之年，也是两个百年目标交汇与转换之年。为了让我校师生快速了解国内外学术前沿、经典及热点，图书馆学科服务团队特开辟此栏目，利用 WOS/ESI/Incites、Scopus/SciVal 等权威数据库和分析工具筛选研究前沿，或跟踪重要学术网站获取最新学术动态，分专题进行编译报道。因学科专业所限，难免出错，敬请批评指正。同时，我们也面向全校师生征集关注的领域和专题。

本期推荐报道 Nature、Science 期刊上物理领域的最新论文。

CONTACT US

联系电话：025-52090336-817

办公地址：李文正图书馆 B401 室

本期编辑：刘丽娟

本期审核：陆　美

美国 Science（《科学》）、英国 Nature（《自然》）及美国 Cell（《细胞》）是国际公认的三大享有最高学术声誉的科技期刊，发表在这三大期刊上的论文简称 CNS 论文。本次精选 2021 年 4 月 Science 和 Nature 中的部分物理领域论文，详细情况如下。

物理 4 月 Science 论文

[1]**Observation of a non-Hermitian phase transition in an optical quantum gas**

光学量子气体中非厄米相变的观察

出版信息：Science 02 Apr 2021:Vol. 372, Issue 6537, pp. 88-91

作者：Fahri Emre Öztürk, Tim Lappe, Göran Hellmann, Julian Schmitt, Jan Klaers, Frank Vewinger, et al.

第一作者单位：Institut für Angewandte Physik, Universität Bonn, Wegelerstr. 8, 53115 Bonn, Germany.

全文链接：https://science.sciencemag.org/content/372/6537/88

Abstract：Quantum gases of light, such as photon or polariton condensates in optical microcavities, are collective quantum systems enabling a tailoring of dissipation from, for example, cavity loss. This characteristic makes them a tool to study dissipative phases, an emerging subject in quantum many-body physics. We experimentally demonstrate a non-Hermitian phase transition of a photon Bose-Einstein condensate to a dissipative phase characterized by a biexponential decay of the condensate’s second-order coherence. The phase transition occurs because of the emergence of an exceptional point in the quantum gas. Although Bose-Einstein condensation is usually connected to lasing by a smooth crossover, the observed phase transition separates the biexponential phase from both lasing and an intermediate, oscillatory condensate regime. Our approach can be used to study a wide class of dissipative quantum phases in topological or lattice systems.

摘要翻译：光的量子气体，例如光学微腔中的光子或极化激元凝聚，是一种集合量子系统，能够通过诸如空腔损耗来调节耗散。这一特性使它们成为研究耗散相的工具，耗散相是量子多体物理学中的一个新兴课题。研究组实验证明了光子玻色-爱因斯坦凝聚的非厄米相转到二阶相干双指数衰减的耗散相。相变的发生是因为量子气体中出现了一个异常点。虽然玻色-爱因斯坦凝聚常通过平滑交叉连接到激光上，但观察到的相变将双指数相位从激光和一个中间振荡凝聚区中分离出来。研究组的方法可用于研究拓扑或晶格系统中的大量耗散量子相。

文中插图：

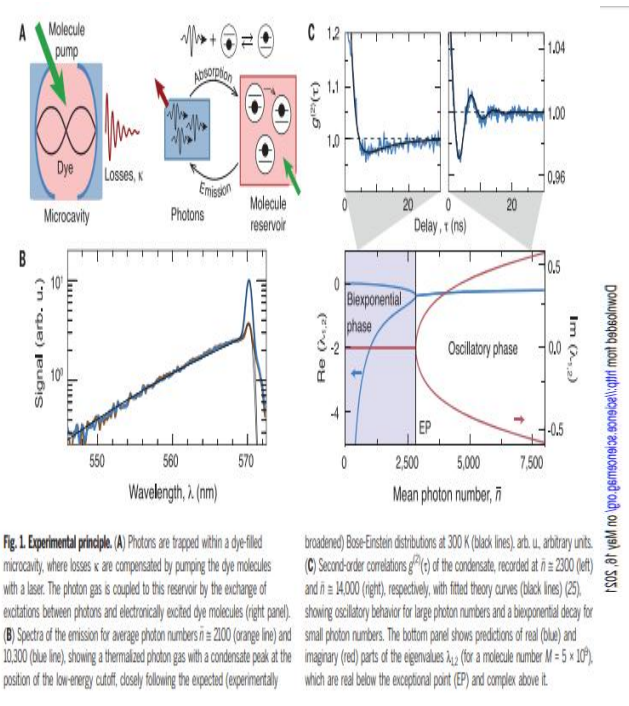

Fig. 1. Experimental principle. (A) Photons are trapped within a dye-filled microcavity, where losses κ are compensated by pumping the dye molecules with a laser. The photon gas is coupled to this reservoir by the exchange of excitations between photons and electronically excited dye molecules (right panel). (B) Spectra of the emission for average photon numbers $\bar{n} \approx 2200$ (orange line) and 10,300 (blue line), showing a thermalized photon gas with a condensate peak at the position of the low-energy cutoff, closely following the expected (experimentally broadened) Bose-Einstein distributions at 300 K (black lines). arb. u., arbitrary units. (C) Second-order correlations $g^{(2)}(\tau)$ of the condensate, recorded at $\bar{n} \approx 2300$ (left) and $\bar{n} \approx 14{,}000$ (right), respectively, with fitted theory curves (black lines) (25), showing oscillatory behavior for large photon numbers and a biexponential decay for small photon numbers. The bottom panel shows predictions of real (blue) and imaginary (red) parts of the eigenvalues $\lambda_{1,2}$ (for a molecule number $M = 5 \times 10^8$), which are real below the exceptional point (EP) and complex above it.

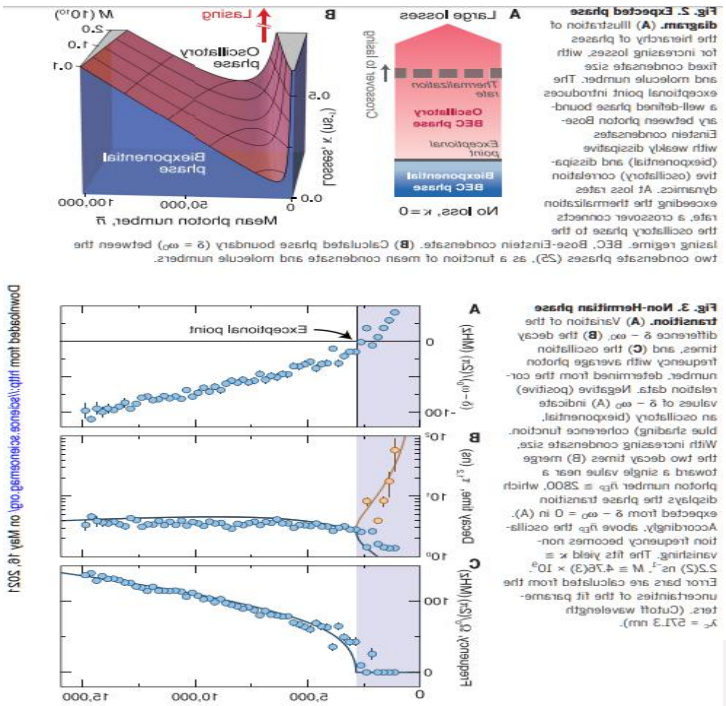

Fig. 2. Expected phase diagram. (A) Illustration of the hierarchy of phases for increasing losses, with fixed condensate size and molecule number. The exceptional point introduces a well-defined phase boundary between photon Bose-Einstein condensates with weakly dissipative (biexponential) and dissipative (oscillatory) correlation dynamics. At loss rates exceeding the thermalization rate, a crossover connects the oscillatory phase to the lasing regime. BEC, Bose-Einstein condensate. (B) Calculated phase boundary ($\delta = \omega_0$) between the two condensate phases (25), as a function of mean condensate and molecule numbers.

Fig. 3. Non-Hermitian phase transition. (A) Variation of the difference $\delta - \omega_0$. (B) the decay times, and (C) the oscillation frequency with average photon number, determined from the correlation data. Negative (positive) values of $\delta - \omega_0$ (A) indicate an oscillatory (biexponential, blue shading) coherence function. With increasing condensate size, the two decay times (B) merge toward a single value near a photon number $\bar{n}_{EP} \approx 2800$, which displays the phase transition expected from $\delta - \omega_0 = 0$ in (A). Accordingly, above $\bar{n}_{EP}$ the oscillation frequency becomes non-vanishing. The fits yield $\kappa \approx 2.2(2)\,\mathrm{ns}^{-1}$, $M \approx 4.7(3) \times 10^8$. Error bars are calculated from the uncertainties of the fit parameters. (Cutoff wavelength $\lambda_c = 573.3$ nm).

[2]Nonlinear tuning of PT symmetry and non-Hermitian topological states

PT 对称与非厄米拓扑态的非线性调谐

出版信息：Science 02 Apr 2021:Vol. 372, Issue 6537, pp. 72-76

作者：Shiqi Xia, Dimitrios Kaltsas, Daohong Song, Ioannis Komis, Jingjun Xu, Alexander Szameit, et al.

第一作者单位：MOE Key Laboratory of Weak-Light Nonlinear Photonics, TEDA Applied Physics Institute and School of Physics, Nankai University, Tianjin 300457, China.

国内相关报道：http://news.nankai.edu.cn/ywsd/system/2021/04/02/030045228.shtml

全文链接：https://science.sciencemag.org/content/372/6537/72

Abstract：Topology, parity-time (PT) symmetry, and nonlinearity are at the origin of many fundamental phenomena in complex systems across the natural sciences, but their mutual interplay remains unexplored. We established a nonlinear non-Hermitian topological platform for active tuning of PT symmetry and topological states. We found that the loss in a topological defect potential in a non-Hermitian photonic lattice can be tuned solely by nonlinearity, enabling the transition between PT-symmetric and non–PT-symmetric regimes and the maneuvering of topological zero modes. The interaction between two apparently antagonistic effects is revealed: the sensitivity close to exceptional points and the robustness of non-Hermitian topological states. Our scheme using single-channel control of global PT symmetry and topology via local nonlinearity may provide opportunities for unconventional light manipulation and device applications.

摘要翻译：在自然科学的复杂系统中，拓扑结构、宇称时间（PT）对称性和非线性是许多基本现象的起源，但它们之间的相互作用尚未明确。研究组建立了一个非线性非厄米拓扑平台，用于 PT 对称性和拓扑态的主动调谐。他们发现，非厄米光子晶格中拓扑缺陷势的损耗可完全通过非线性调谐，实现 PT 对称和非 PT 对称区域之间的转换，并引导拓扑零模。研究组还揭示了两种明显对抗效应间的相互作用，即对异常点的敏感性和非厄米拓扑态的鲁棒性。该方案利用局部非线性的 PT 对称和拓扑结构的单通道控制，为非常规的光操作和器件应用提供了机会。

文中插图：

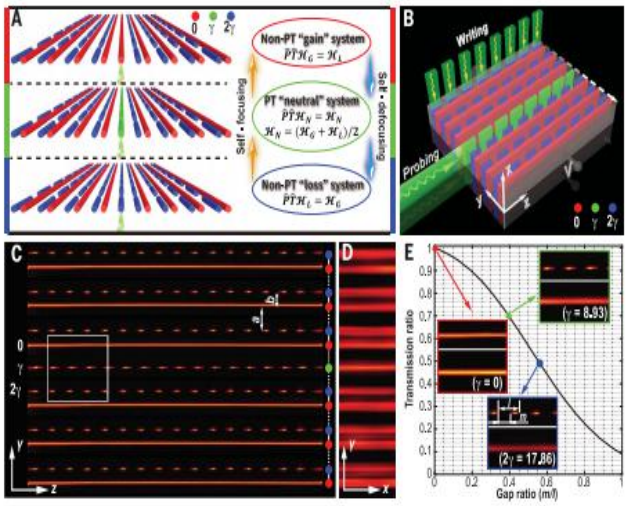

Fig. 1. Experimental realization of NNH-SSHs for nonlinear tuning of PT symmetry and topological states. (**A**) Illustration of a passive PT-symmetric "neutral" SSH lattice (middle) switched to a non-PT "gain" lattice (top) or a non-PT "loss" lattice (bottom) by local nonlinearity at the topological defect. The switching direction can be readily reversed. Red, green, and blue cylinders and dots represent "gain," "neutral," and "loss" lattice sites (γ is the loss coefficient); colored bars denote different stages of the NNH-SSHs. The Hamiltonian relations are illustrated for corresponding active non-Hermitian systems (*29*). (**B**) Schematic for cw-laser writing and probing the lattices. A dashed white arrow marks the writing sequence. (**C**) Side view of the writing beam pattern, where a = 22.8 μm and b = 15.2 μm represent waveguide spacing for the dimer lattice. (**D**) The written NNH-SSH examined by a broad plane-wave beam. (**E**) Plot of intensity transmission ratio as a function of the gap ratio in a single waveguide obtained from simulation. Insets show side views of a waveguide portion taken from the experiment in (C) at m/l = 0 (red), 0.40 (green), and 0.56 (blue), where in each inset a single writing beam is shown at the top and the guided output probe beam at the bottom.

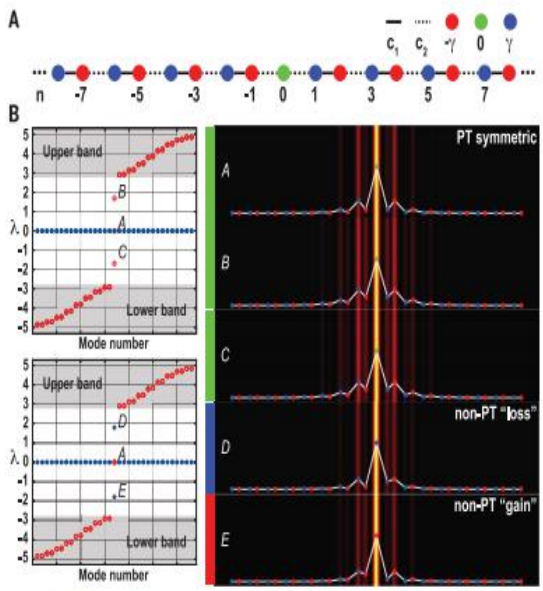

Fig. 2. Calculated non-Hermitian topological interface states tuned by nonlinearity. (**A**) Illustration of an active PT-symmetric SSH with an interface topological defect located at site n = 0. Colored dots represent different lattice sites. (**B**) Left: Calculated eigenvalues λ for a finite lattice with 33 sites. Red circles and blue dots denote real and imaginary parts of the eigenvalues, respectively; shaded regions illustrate the band structure of an infinite lattice. Right: The corresponding eigenmode profiles, where the eigenvalues for points A to E are obtained with propagation constants β_0 = 0, 2, −2, 2i, and −2i while keeping β for all other waveguides unchanged. Color codes for different waveguides are the same as in Fig. 1.

[3]Enhanced x-ray emission coinciding with giant radio pulses from the Crab Pulsar

增强 X 射线发射与蟹状星云脉冲星发出的巨大射电脉冲相吻合

出版信息：Science 09 Apr 2021:Vol. 372, Issue 6538, pp. 187-190

作者：Teruaki Enoto, Toshio Terasawa, Shota Kisaka, Shuta J. Tanaka, etc.

第一作者单位：Cluster for Pioneering Research, RIKEN, Wako 351-0198, Japan.

全文链接：https://science.sciencemag.org/content/372/6538/187

Abstract：Pulsars are spinning, magnetized neutron stars that are observed as a regular sequence of radio pulses. Most pulses are of consistent intensity, but occasionally one is brighter by orders of magnitude. The cause of these unpredictable giant radio pulses (GRPs) is unknown. Enoto et al. observed the Crab Pulsar simultaneously with x-ray and radio telescopes. They found that x-ray emission during GRPs was slightly brighter than that during normal pulses. Comparing the radio and x-ray enhancements provides constraints on the GRP emission mechanism and the possible connections with other transient radio phenomena.

摘要翻译：脉冲星是旋转的、磁化的中子星，观测到的是有规律的射电脉冲序列。大多数脉冲的强度都是一致的，但偶尔有一个脉冲的亮度要高几个数量级。这些不可预测的巨型无线电脉冲（GRPs）的成因尚不清楚。作者同时用 X 射线和射电望远镜观测蟹状星云脉冲星。他们发现 GRPs 发出的 X 射线比正常脉冲发出的要强一些。比较射电和 X 射线增强对 GRP 发射机制以及可能与其他瞬态射电现象的联系提供了约束。

文中插图：

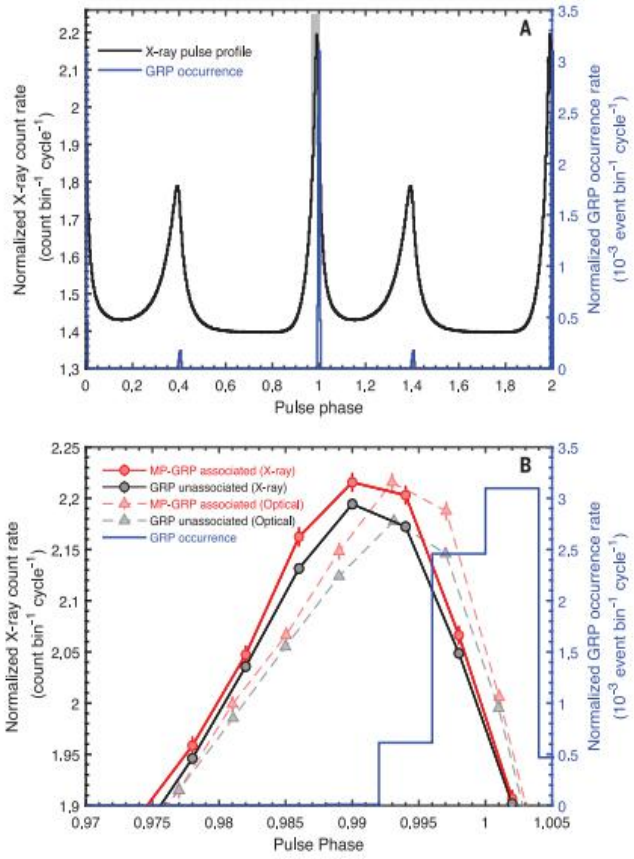

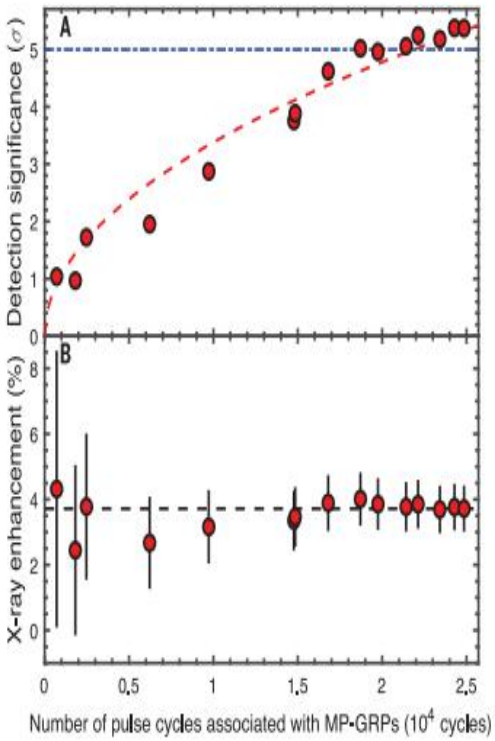

Fig. 2. Growth curves of the detection significance and x-ray enhancement. (**A**) Detection significance as a function of the accumulated number of rotation cycles observed to be associated with MP-GRPs. Data accumulation was performed chronologically, i.e., each data point represents all the *NICER* data up to that epoch. The horizontal blue dot-dashed line is the 5σ detection significance level, and the red dashed curve is the best-fitting model: the square root of the cycle number. (**B**) Same as (A) but for the degree of x-ray enhancement. The horizontal dashed line shows the 3.8% enhancement ratio derived from the entire dataset. Error bars are statistical 1σ uncertainties.

[4]Gate-controlled BCS-BEC crossover in a two-dimensional superconductor

二维超导体中的门控 BCS-BEC 交叉

出版信息: Science 09 Apr 2021:Vol. 372, Issue 6538, pp. 190-195

作者： Yuji Nakagawa, Yuichi Kasahara, Takuya Nomoto, Ryotaro Arita, Tsutomu Nojima, Yoshihiro Iwasa

第一作者单位： Department of Applied Physics, University of Tokyo, Hongo 7-3-1, Bunkyo-ku, Tokyo 113-8656, Japan.

全文链接： https://science.sciencemag.org/content/372/6538/190

Abstract： In conventional superconductors, the electron pairs responsible for superconductivity are large and overlapping. Starting from this so-called Bardeen-Cooper-Schrieffer (BCS) limit, increasing interactions can set the system on a path of crossover to the opposite limit of small, tightly bound electron pairs that undergo Bose-Einstein condensation (BEC). Nakagawa et al. intercalated lithium ions into the insulating material zirconium nitride chloride, varying the carrier density across a large range. This induced superconductivity and enabled the system to enter the crossover regime between the BCS and BEC limits.

摘要翻译： 在传统的超导体中，导致超导性的电子对是大而重叠的。从巴丁-库珀-徐瑞弗（BCS）极限开始，不断增加的相互作用可以使系统在交叉路径上达到小的、紧密束缚的电子对的相反极限，这些电子对经历玻色-爱因斯坦凝聚（BEC）作者将锂离子插入绝缘材料氯化氮化锆中，在很大范围内改变载流子密度。这引起了超导性，并使系统能够进入 BCS 和 BEC 极限之间的交叉区。

文中插图：

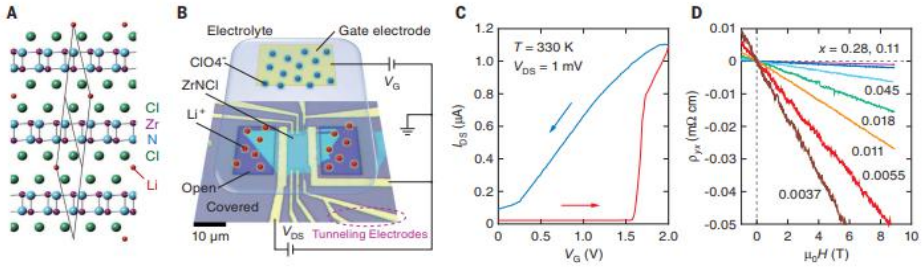

Fig. 1. Gate-controlled intercalation in a ZrNCl device. (**A**) Side view of Li_xZrNCl crystal structure. Solid lines represent the rhombohedral unit cell. (**B**) Schematic illustration of the ionic-gating device based on a real optical micrograph of a ZrNCl single-crystal flake and patterned electrodes. Narrow contacts are prepared for the tunneling spectroscopy measurements. PMMA covers the whole device except for the outer area of the flake and the gate electrode. The electrolyte containing $LiClO_4$ is dropped onto the device. A gate voltage V_G is applied to the electrolyte, and lithium cations and ClO_4 anions move oppositely. Lithium cations intercalate from the sides of the flake. (**C**) Source-drain current I_{DS} of the device in intercalation operation. During the forward sweep of V_G (red), I_{DS} increases steeply, whereas the change of I_{DS} is gradual in the backward scan (blue). V_G is swept at a speed of 10 mV/s. (**D**) Antisymmetrized transverse resistivity at 150 K for various values of the Li content x. The linear slope is used to determine x.

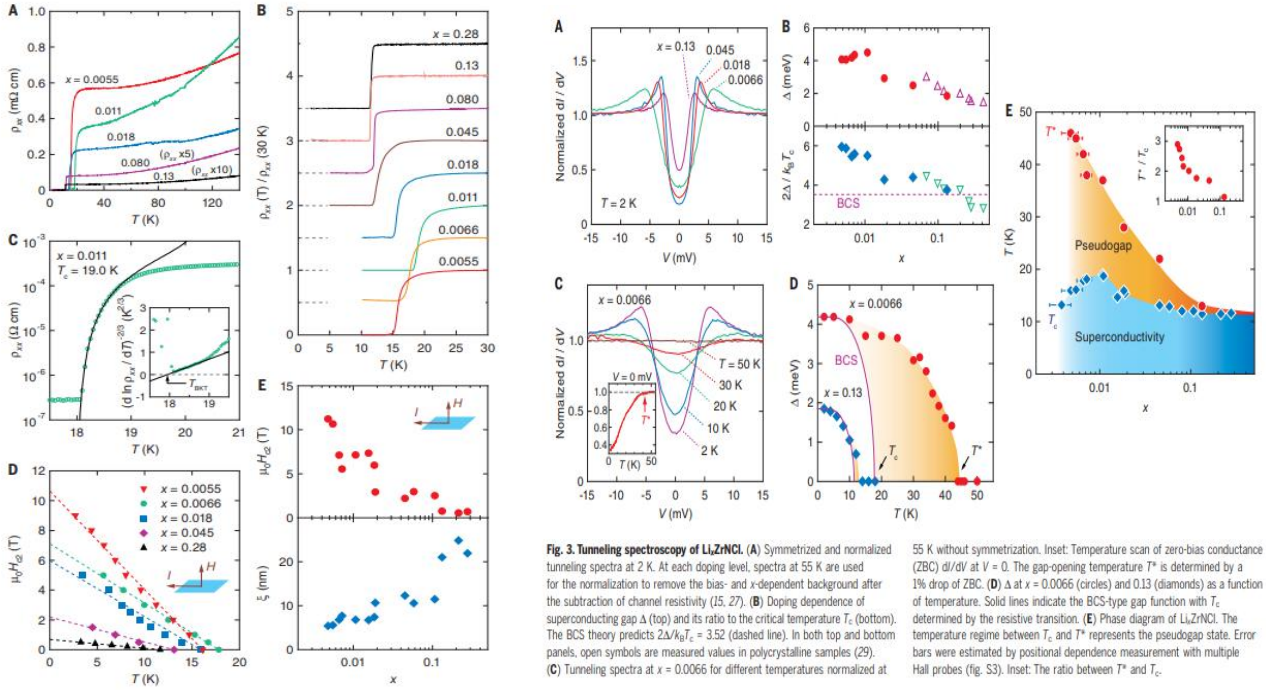

Fig. 3. Tunneling spectroscopy of Li_xZrNCl. (**A**) Symmetrized and normalized tunneling spectra at 2 K. At each doping level, spectra at 55 K are used for the normalization to remove the bias- and x-dependent background after the subtraction of channel resistivity (*15*, *27*). (**B**) Doping dependence of superconducting gap Δ (top) and its ratio to the critical temperature T_c (bottom). The BCS theory predicts $2\Delta/k_BT_c = 3.52$ (dashed line). In both top and bottom panels, open symbols are measured values in polycrystalline samples (*29*). (**C**) Tunneling spectra at $x = 0.0066$ for different temperatures normalized at 55 K without symmetrization. Inset: Temperature scan of zero-bias conductance (ZBC) dI/dV at $V = 0$. The gap-opening temperature T^* is determined by a 1% drop of ZBC. (**D**) Δ at $x = 0.0066$ (circles) and 0.13 (diamonds) as a function of temperature. Solid lines indicate the BCS-type gap function with T_c determined by the resistive transition. (**E**) Phase diagram of Li_xZrNCl. The temperature regime between T_c and T^* represents the pseudogap state. Error bars were estimated by positional dependence measurement with multiple Hall probes (fig. S3). Inset: The ratio between T^* and T_c.

[5]Josephson junction infrared single-photon detector

约瑟夫森结红外单光子探测器

出版信息：Science　23 Apr 2021:Vol. 372, Issue 6540, pp. 409-412

作者：Evan D. Walsh, Woochan Jung, Gil-Ho Lee, Dmitri K. Efetov, Bae-Ian Wu, K.-F. Huang, et

第一作者单位：Department of Electrical Engineering and Computer Science, Massachusetts Institute of Technology, Cambridge, MA 02139, USA.

全文链接：https://science.sciencemag.org/content/372/6540/409

Abstract：Josephson junctions are superconducting devices used as high-sensitivity magnetometers and voltage amplifiers as well as the basis of high-performance cryogenic computers and superconducting quantum computers. Although device performance can be degraded by the generation of quasiparticles formed from broken Cooper pairs, this phenomenon also opens opportunities to sensitively detect electromagnetic radiation. We demonstrate single near-infrared photon detection by coupling photons to the localized surface plasmons of a graphene-based Josephson junction. Using the photon-induced switching statistics of the current-biased device, we reveal the critical role of quasiparticles generated by the absorbed photon in the detection mechanism. The photon sensitivity will enable a high-speed, low-power optical interconnect for future superconducting computing architectures.

摘要翻译：约瑟夫森结是用于高灵敏度磁强计和电压放大器的超导器件，也是高性能低温计算机和超导量子计算机的基础。虽然因库珀对断裂产生的准粒子会降低器件性能，但这种现象也为灵敏探测电磁辐射提供了机会。研究组演示了通过将光子耦合到石墨烯基约瑟夫森结的局域表面等离子体来探测单个近红外光子。利用电流偏置器件的光子诱导开关统计，研究组揭示了吸收光子产生的准粒子在探测机制中的关键作用。光子灵敏度将为未来的超导计算架构提供高速、低功耗的光互连。

文中插图：

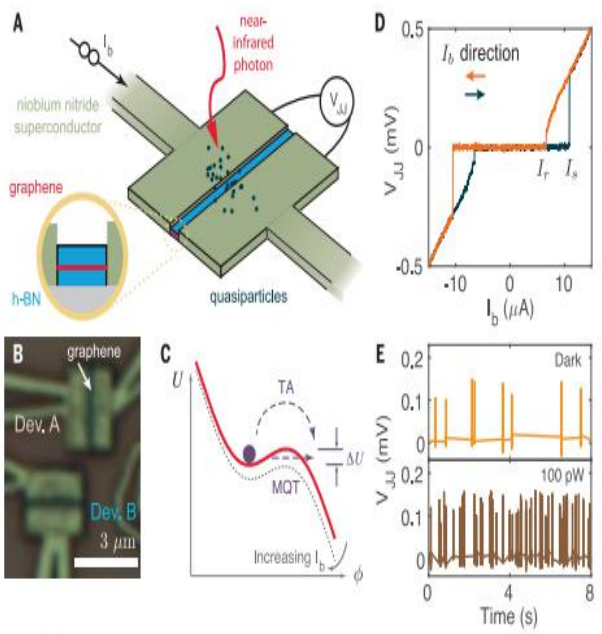

Fig. 1. Current-biased JJ as a SPD. (**A**) QPs are generated as incident photons break Cooper pairs and trigger the JJ to switch. (**B**) Optical image of two graphene-based JJs. (**C**) The behavior of the current-biased JJ can be described by a macroscopic quantum phase particle subjected to a tilted-washboard potential in the RCSJ model. QPs can assist the phase particle to move out of the trapping potential, switching the JJ to a normal resistive state. (**D**) Typical IV curve displaying the switching and retrapping of JJ at I_s and I_r, respectively. (**E**) Switching events in dark and 100 pW of 1550-nm light at I_b = 10.90 μA.

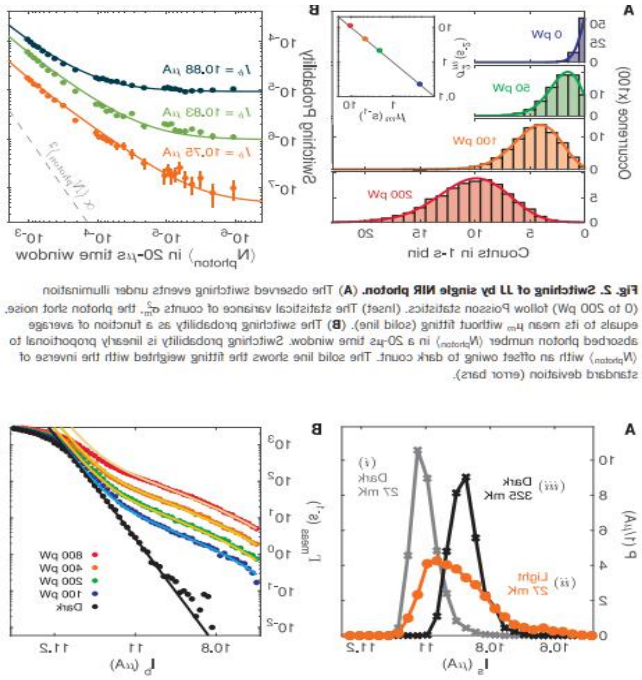

Fig. 2. Switching of JJ by single NIR photon. (**A**) The observed switching events under illumination (0 to 200 pW) follow Poisson statistics. (Inset) The statistical variance of counts $\sigma^2_{N_{photon}}$, the photon shot noise, equals to its mean $\mu_{N_{photon}}$ without fitting (solid line). (**B**) The switching probability as a function of average absorbed photon number (N_{photon}) in a 20-μs time window. Switching probability is linearly proportional to (N_{photon}) with an offset owing to dark count. The solid line shows the fitting weighted with the inverse of standard deviation (error bars).

Fig. 3. Switching mechanism. (**A**) The distribution of switching current I_s by ramping up I_b at 1 μA/s under three conditions: (i) at 27 mK in the absence and (ii) the presence (orange) of 100 pW of 1550-nm light and (iii) at 325 mK in the absence of light. (ii) and (iii) have the same average I_s but different shapes, thus ruling out steady heating from laser power. (**B**) The switching rate as a function of bias current with various incident laser powers. The points are measured values, the black line is the best fit of the MQT process to Γ_{meas} without light, and the color lines are modeled results from photon-enhanced Γ_{light}^{esc}. The linearity of the data on a semilog plot indicates a momentary elevation of the escape energy by the photon.

[6]Higher-dimensional supersymmetric microlaser arrays

高维超对称微激光阵列

出版信息：Science 23 Apr 2021:Vol. 372, Issue 6540, pp. 403-408

作者：Xingdu Qiao, Bikashkali Midya, Zihe Gao, Zhifeng Zhang, Haoqi Zhao, Tianwei Wu, et al.

第一作者单位：Department of Electrical and Systems Engineering, University of Pennsylvania, Philadelphia, PA 19104, USA.

全文链接：https://science.sciencemag.org/content/372/6540/403

Abstract：The nonlinear scaling of complexity with the increased number of components in integrated photonics is a major obstacle impeding large-scale, phase-locked laser arrays. Here, we develop a higher-dimensional supersymmetry formalism for precise mode control and nonlinear power scaling. Our supersymmetric microlaser arrays feature phase-locked coherence and synchronization of all of the evanescently coupled microring lasers—collectively oscillating in the fundamental transverse supermode—which enables high-radiance, small-divergence, and single-frequency laser emission with a two-orders-of-magnitude enhancement in energy density. We also demonstrate the feasibility of structuring high-radiance vortex laser beams, which enhance the laser performance by taking full advantage of spatial degrees of freedom of light. Our approach provides a route for designing large-scale integrated photonic systems in both classical and quantum regimes.

摘要翻译：随着集成光子学元件数量的增加，复杂度的非线性缩放是阻碍大规模锁相激光阵列的主要障碍。研究组开发了一种高维超对称形式，用于精确模式控制和非线性功率缩放。这种超对称微激光阵列具有所有倏逝波耦合微环激光器的锁相相干性和同步性，可在基本横向超模中集体振荡，从而实现高辐射、小发散和单频激光发射，且能量密度提高两个数量级。研究组还证明了构造高辐射涡旋激光束的可行性，即充分利用光的空间自由度提高激光器的性能。该研究方法为在经典和量子两种状态下设计大规模集成光子系统提供了一条新途径。

文中插图：

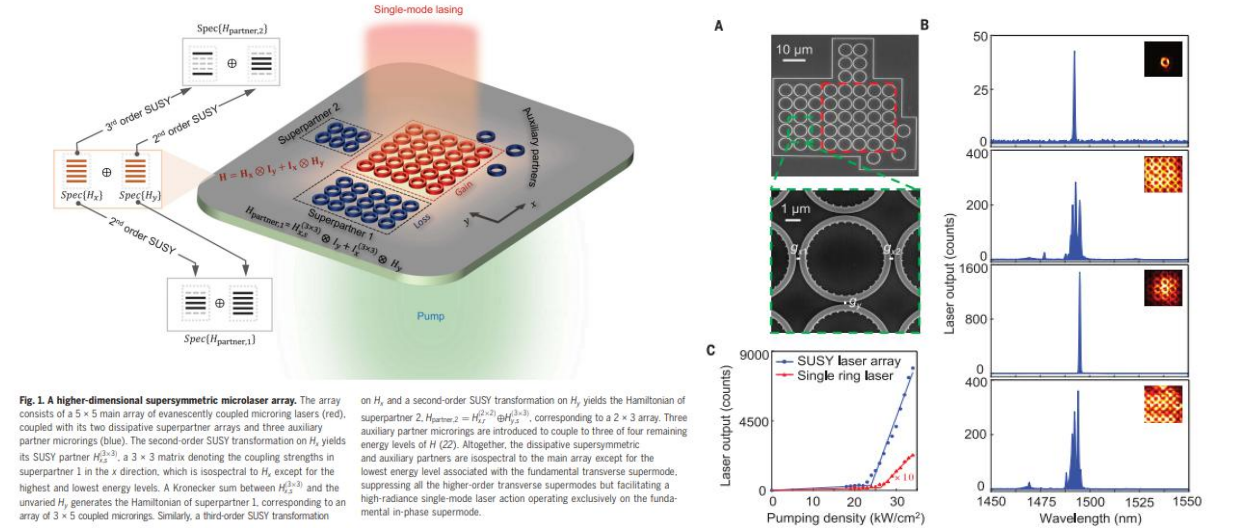

Fig. 1. A higher-dimensional supersymmetric microlaser array. The array consists of a 5 × 5 main array of evanescently coupled microring lasers (red), coupled with its two dissipative superpartner arrays and three auxiliary partner microrings (blue). The second-order SUSY transformation on H_x yields its SUSY partner $H_{SX}^{(3\times3)}$, a 3 × 3 matrix denoting the coupling strengths in superpartner 1 in the x direction, which is isospectral to H_x except for the highest and lowest energy levels. A Kronecker sum between $H_{SX}^{(3\times3)}$ and the unvaried H_y generates the Hamiltonian of superpartner 1, corresponding to an array of 3 × 5 coupled microrings. Similarly, a third-order SUSY transformation on H_x and a second-order SUSY transformation on H_y yields the Hamiltonian of superpartner 2, $H_{\text{partner},2} = H_{SY}^{(2\times2)} \oplus H_{SX}^{(3\times3)}$, corresponding to a 2 × 3 array. Three auxiliary partner microrings are introduced to couple to three of four remaining energy levels of H (22). Altogether, the dissipative supersymmetric and auxiliary partners are isospectral to the main array except for the lowest energy level associated with the fundamental transverse supermode, suppressing all the higher-order transverse supermodes but facilitating a high-radiance single-mode laser action operating exclusively on the fundamental in-phase supermode.

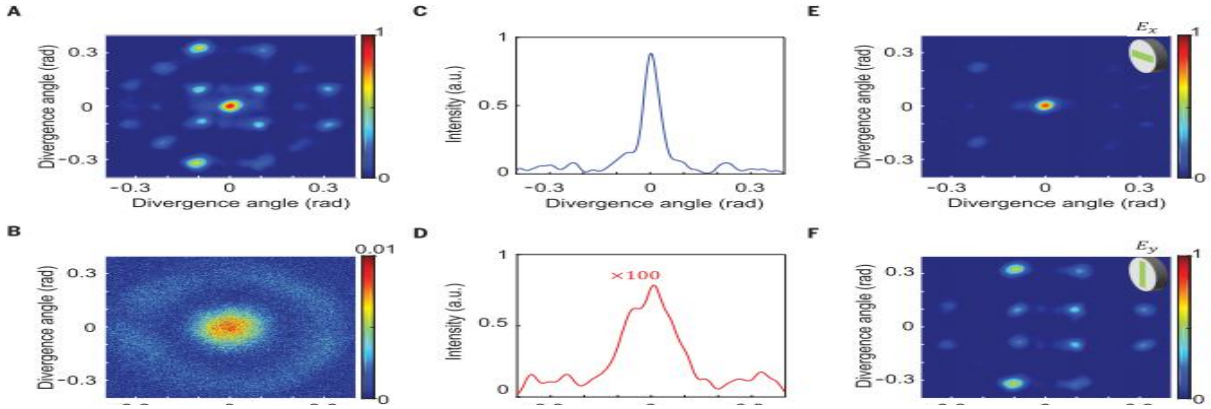

[7]Realization of a multinode quantum network of remote solid-state qubits

远程固态量子比特的多态量子网络的实现

出版信息：Science 16 Apr 2021:Vol. 372, Issue 6539, pp. 259-264

作者：M. Pompili, S. L. N. Hermans, S. Baier, H. K. C. Beukers, et al.

第一作者单位：QuTech, Delft University of Technology, 2628 CJ Delft, Netherlands.

全文链接：https://science.sciencemag.org/content/372/6539/259

Abstract：The distribution of entangled states across the nodes of a future quantum internet will unlock fundamentally new technologies. Here, we report on the realization of a three-node entanglement-based quantum network. We combine remote quantum nodes based on diamond communication qubits into a scalable phase-stabilized architecture, supplemented with a robust memory qubit and local quantum logic. In addition, we achieve real-time communication and feed-forward gate operations across the network. We demonstrate two quantum network protocols without postselection: the distribution of genuine multipartite entangled states across the three nodes and entanglement swapping through an intermediary node. Our work establishes a key platform for exploring, testing, and developing multinode quantum network protocols and a quantum network control stack.

摘要翻译：纠缠态在未来量子互联网节点上的分布将开启根本性的新技术。在此，我们报告一个基于三节点纠缠的量子网络的实现。我们将基于金刚石通信量子位的远程量子节点组合成一个可扩展的相位稳定架构，并辅以健壮的存储量子位和局部量子逻辑。此外，我们还实现了网络上的实时通讯和前馈门运作。我们证明了两个没有后选择的量子网络协议：真正的多部纠缠态在三个节点上的分布和纠缠态通过一个中间节点进行交换。我们的工作为探索、测试和开发多态量子网络协议和量子网络控制栈奠定了关键平台。

文中插图：

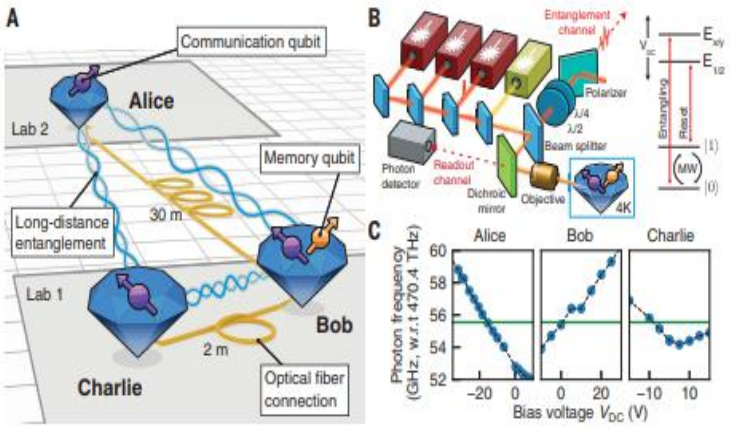

Fig. 1. The three-node quantum network. (**A**) Layout of the network. Three nodes, labeled Alice, Bob, and Charlie, are located in two separate labs. Each node contains an NV center communication qubit (purple). At Bob, an additional nuclear spin qubit (orange) is used in the presented experiments. Fiber connections between the nodes (lengths indicated) enable remote entanglement generation on the links Alice-Bob and Bob-Charlie, which, combined with local quantum logic, allow for entanglement to be shared between all nodes (wiggly lines). (**B**) On the left is a simplified schematic of the optical setup at each node [see fig. S1, table S1, and (*27*) for additional details]. On the right is a diagram of the relevant levels of the electronic spin qubit, showing optical transitions for remote entanglement generation and readout ("entangling"), qubit reset ("reset"), and resonant microwaves ("MW") for qubit control (see figs. S2 and S3 for additional details). The memory qubit at Bob is initialized, controlled, and read out via the electronic qubit (fig. S4). Optical transition frequencies are tuned via the dc bias voltages (V_{DC}). $\lambda/2$ ($\lambda/4$) is a half-waveplate (quarter-waveplate); $E_{x/y}$ and $E_{1/2}$ are electronic excited states. (**C**) Tuning of the optical "entangling" transition at each of the three nodes. The solid line is the working point, 470.45555 THz; the dashed line is a guide to the eye. w.r.t., with respect to.

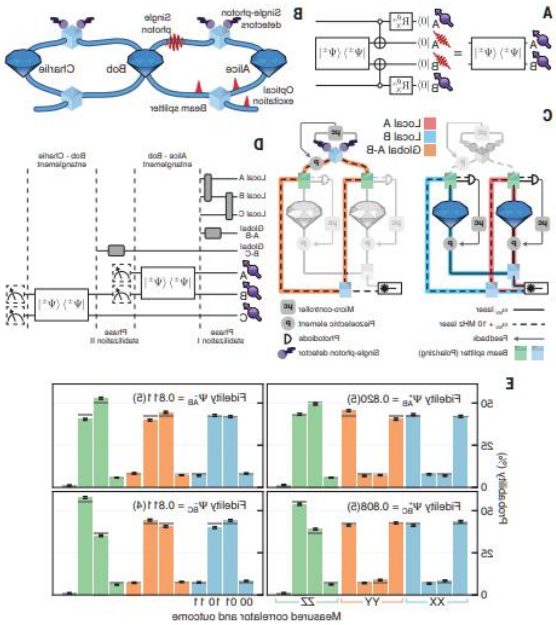

Fig. 2. Establishing remote entanglement in a network architecture. (**A**) Circuit diagram of the single-photon entanglement protocol, where $R_{\vec{n}}^{\theta}$ is a rotation around the x axis with angle θ_{α}, $\theta_{\alpha} = 2\cos^{-1}(\sqrt{\alpha})$. (**B**) Sketch of three quantum network nodes in line configuration, showing the two effective interferometers. (**C**) Phase stabilization diagram of the Alice-Bob link, highlighting the local interferometers (left) and the global interferometer (right). See (*27*) for further details. (**D**) Experimental sequence to generate Bell pairs on both Alice-Bob (A-B) and Bob-Charlie (B-C) links. Dashed boxes display measurements used in (**E**). (**E**) Correlation measurements on entangled states on A-B (top) and B-C (bottom) links. The left plots correspond to $|\Psi^+\rangle$ states; the right plots correspond to $|\Psi^-\rangle$ states. Shown are observed probabilities for outcomes (from left to right) 00, 01, 10, and 11 for correlation measurements in the bases XX (blue), YY (orange), and ZZ (green). Gray bars depict values from the theoretical model. Error bars indicate one standard deviation.

[8]Gapped magnetic ground state in quantum spin liquid candidate κ-(BEDT-TTF)2Cu2(CN)3

量子自旋液体候选 κ-(BEDT-TTF)2Cu2(CN)3 的缝隙磁基态

出版信息：Science 16 Apr 2021:Vol. 372, Issue 6539, pp. 276-279

作者：Björn Miksch, Andrej Pustogow, Mojtaba Javaheri Rahim, Andrey A. Bardin, et al.

第一作者单位：Physikalisches Institut, Universität Stuttgart, 70569 Stuttgart, Germany.

全文链接：https://science.sciencemag.org/content/372/6539/276

Abstract：Geometrical frustration, quantum entanglement, and disorder may prevent long-range ordering of localized spins with strong exchange interactions, resulting in an exotic state of matter. κ-(BEDT-TTF)2Cu2(CN)3 is considered the prime candidate for this elusive quantum spin liquid state, but its ground-state properties remain puzzling. We present a multifrequency electron spin resonance (ESR) study down to millikelvin temperatures, revealing a rapid drop of the spin susceptibility at 6 kelvin. This opening of a spin gap, accompanied by structural modifications, is consistent with the formation of a valence bond solid ground state. We identify an impurity contribution to the ESR response that becomes dominant when the intrinsic spins form singlets. Probing the electrons directly manifests the pivotal role of defects for the low-energy properties of quantum spin systems without magnetic order.

摘要翻译：几何挫折、量子纠缠和无序可能会阻止具有强交换作用的局域自旋的长程有序，从而导致物质的奇异状态。κ-(BEDT-TTF)2Cu2(CN)3 被认为是这种难以捉摸的量子自旋液态的主要候选者，但它的基态性质仍然令人费解。我们提出一个毫开尔文温度以下的多频率电子自旋共振（ESR）的研究，揭示了自旋敏感性在 6 k 时的迅速下降。这种自旋间隙的打开，伴随着结构的改变，与固态价键基态的形成是一致的。我们发现当本征自旋形成单线态时，杂质对 ESR 响应的贡献占主导地位。直接探测电子表明了缺陷对于无磁序量子自旋系统的低能量特性的关键作用。

文中插图：

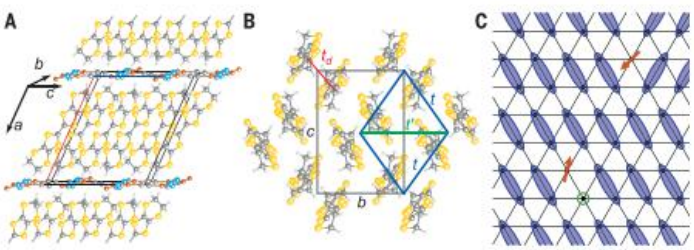

Fig. 1. Crystal structure of the QSL candidate κ-(BEDT-TTF)$_2$Cu$_2$(CN)$_3$. (**A**) Layers of tilted BEDT-TTF dimers in the *bc* plane are separated in *a** direction [*a** ⊥ (*bc*)] by $[Cu_2(CN)_3]^-_\infty$ anion sheets. The colors represent the different atoms in (A) and (B): gray, carbon; yellow, sulfur; white, hydrogen; blue, nitrogen; and red, copper. (**B**) The dimers are internally coupled by the transfer integral t_d and arranged on a slightly distorted triangular lattice. The interdimer transfer integrals *t* and *t'* define the degree of frustration, *t'*/*t* = 0.83. (**C**) Sketch of a valence bond solid state on an *S* = ½ triangular lattice with spin singlets denoted in blue. Domain walls (top right), topological defects, and monomers are expected in real materials. The orange arrows represent unpaired spins caused by random pinning of local moments; vacancies are represented by a green circle.

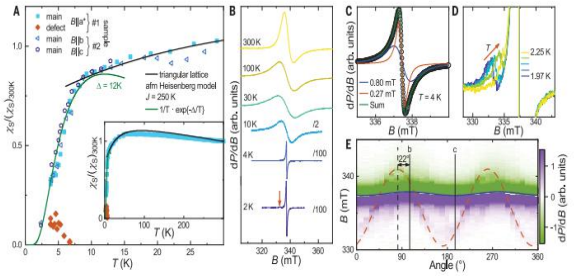

Fig. 2. X-band ESR results of κ-(BEDT-TTF)$_2$Cu$_2$(CN)$_3$. All datasets but one show sample #1; the exception is stated. (**A**) Temperature dependence of the normalized spin susceptibility χ_s measured on two samples along different directions. The data shown for *B*∥*b*,*c* are for sample #2. At elevated temperatures, $\chi_s(T)$ is described by an antiferromagnetic Heisenberg model on a triangular lattice with *J* = 250 K (black line). Below the anomaly at *T** = 6 K, an exponential decay of the main signal evidences the opening of a spin gap Δ = 12 K (green line). The orange diamonds correspond to the signal from defect spins, which becomes obvious for *T* < *T**. Inset: Susceptibility data up to *T* = 300 K for *B*∥*a**. (**B**) Temperature evolution of the X-band spectra with the magnetic field *B*∥*c*. The signal at *T* = 10 K and below is divided by the factors indicated in the figure to account for the increasing peak in dP/dB as the line sharpens. (**C**) Below *T**, an additional narrow component appears, requiring a second Lorentzian function to fit the spectra satisfactorily. As an example, the 4 K data are shown with the respective decomposition. (**D**) Upon cooling below 2.5 K, this new signal separates and shifts to lower resonance fields; we attribute the signal to defect spins not involved in the singlet formation. (**E**) Anisotropy of the ESR resonances of κ-(BEDT-TTF)$_2$Cu$_2$(CN)$_3$. The main signal (solid blue line) is identified by the zero-crossing of dP/dB from positive (green) to negative (violet) and shows a small angular variation of 0.3 mT when measured within the *bc* plane at *T* = 2 K. In contrast, the signal of the defect spins (dashed orange line) has a huge anisotropy of 10 mT offset from the crystallographic *c* direction by an angle of 22° and caused by dipolar interaction to local moments, possibly Cu^{2+} (see text).

Fig. 3. Low-temperature broadband ESR features of κ-(BEDT-TTF)$_2$Cu$_2$(CN)$_3$. (**A**) Coplanar waveguide resonator with mounted sample. The direction of the static magnetic field *B* is shown in black. The microwave magnetic field B_1 (yellow) is subject to absorption by electron spin resonance within the sample. (**B**) *B*∥*c* ESR spectra at 1.1 GHz for different temperatures down to 25 mK. The solid blue line corresponds to the constant main signal B_{main}, whereas the dashed orange line indicates the evolution of the local-moment signal. (**C**) Low-temperature peak positions for varying resonance frequencies and fields.

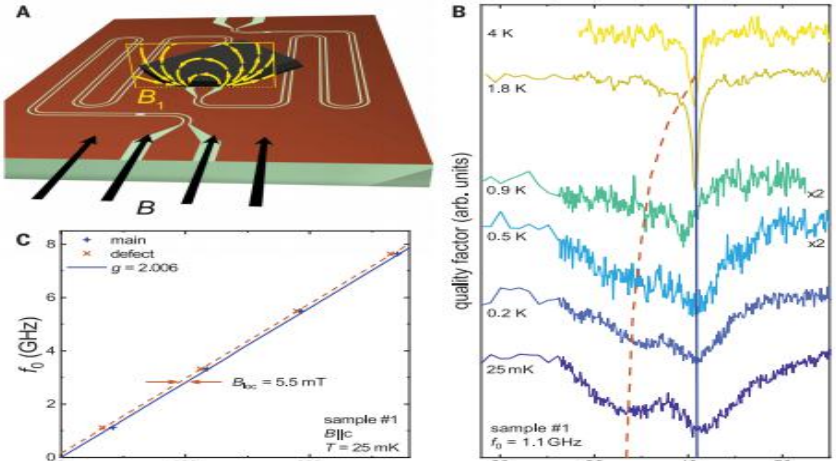

[1]Laser cooling of antihydrogen atoms

反氢原子的激光冷却

出版信息：Nature volume 592, pages 35 – 42 (2021)

作者：C. J. Baker, W. Bertsche

第一作者单位：Department of Physics, College of Science, Swansea University, Swansea, UK

全文链接：https://www.nature.com/articles/s41586-021-03289-6

Abstract：The photon—the quantum excitation of the electromagnetic field—is massless but carries momentum. Here we demonstrate laser cooling of antihydrogen, the antimatter atom consisting of an antiproton and a positron. By exciting the 1S – 2P transition in antihydrogen with pulsed, narrow-linewidth, Lyman-α laser radiation, we Doppler-cool a sample of magnetically trapped antihydrogen. Although we apply laser cooling in only one dimension, the trap couples the longitudinal and transverse motions of the anti-atoms, leading to cooling in all three dimensions. We observe a reduction in the median transverse energy by more than an order of magnitude—with a substantial fraction of the anti-atoms attaining submicroelectronvolt transverse kinetic energies. We also report the observation of the laser-driven 1S – 2S transition in samples of laser-cooled antihydrogen atoms. The observed spectral line is approximately four times narrower than that obtained without laser cooling. The demonstration of laser cooling and its immediate application has far-reaching implications for antimatter studies. A more localized, denser and colder sample of antihydrogen will drastically improve spectroscopic and gravitational studies of antihydrogen in ongoing experiments. Furthermore, the demonstrated ability to manipulate the motion of antimatter atoms by laser light will potentially provide ground-breaking opportunities for future experiments.

摘要翻译：光子——电磁场激发的量子——是无质量的，但携带动量。作者演示了反氢原子的激光冷却，这个反物质原子由一个反质子和一个正电子组成。利用窄线宽脉冲 Lyman-α 激光激发反氢的 1S-2P 跃迁，对磁阱反氢样品进行了多普勒冷却。虽然作者只在一个维度上应用激光冷却，陷阱耦合反原子的纵向和横向运动，导致在所有的三维冷却。作者观察到横能量中值的减少超过一个数量级——有相当一部分反原子获得亚微电子伏横动能。作者还报道了在激光冷却的反氢原子样品中激光驱动 1S-2S 跃迁的观察。观察到的光谱线比没有激光冷却时的光谱线窄约四倍。激光冷却的演示及其立即应用对反物质研究具有深远的意义。一个更局部、密度更大、温度更低的反氢样品将极大地改善正在进行的实验中对反氢的光谱和引力的研究。此外，通过激光操纵反物质原子运动的能力将可能为未来的实验提供突破性的机会。

文中插图：

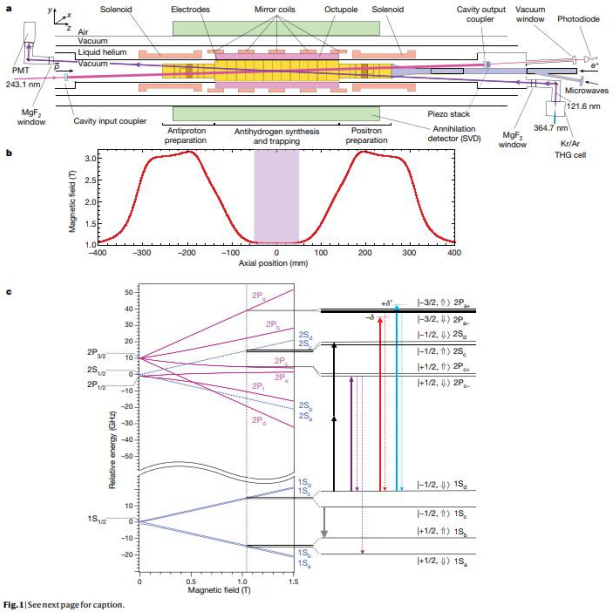

Fig. 1 | See next page for caption.

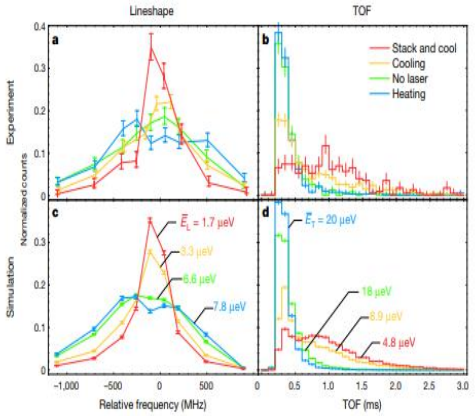

Fig. 2 | Laser cooling of antihydrogen. The spectral lineshapes and the TOF distributions, obtained during the probing phase by detecting antihydrogen annihilations resulting from laser-induced spin flips. In all cases, the curves are drawn to guide the eye. **a**, The experimental lineshapes given by the number of annihilation counts within a TOF time window of 0 to 3 ms, as a function of the probe laser frequency relative to the resonant frequency. **b**, TOF distributions representing the time between the nanosecond-scale probe laser pulse and the detection of the annihilation. Events with an axial annihilation position between +10 cm and −10 cm are plotted. The distributions are compared for the experimental series given in Table 1: the no-laser series (green); the heating series with a detuning of approximately +160 MHz (blue); the cooling series with a −240-MHz detuning (orange); and the 'stack and cool' series where a −230-MHz detuning was applied during both the stacking phase and the cooling phase (red). **c**, **d**, The corresponding simulations for the lineshapes (**c**) and the TOF distributions (**d**). Each distribution is normalized to its total number of counts, and the error bars represent 1 s.d. counting statistical uncertainties. The values labelled $\bar{E}_L$ and $\bar{E}_T$ represent the mean of 'true' longitudinal and transverse energies, respectively, of the simulated atoms at the time of the spin-flip transitions. See text and Methods.

[2]Stabilization of liquid instabilities with ionized gas jets

电离气体射流对液体不稳定性的稳定

出版信息：Nature volume 592, pages 49 – 53 (2021)

作者：Sanghoo Park, Wonho Choe, Hyungyu Lee, Joo Young Park, Jinwoo Kim, Se Youn Moon & Uroš Cvelbar

第一作者单位：Institute of Plasma Technology, Korea Institute of Fusion Energy, Gunsan, Republic of Korea

全文链接：https://www.nature.com/articles/s41586-021-03359-9

Abstract: Impinging gas jets can induce depressions in liquid surfaces, a phenomenon familiar to anyone who has observed the cavity produced by blowing air through a straw directly above a cup of juice. Here we demonstrate the stabilization of such instabilities by weakly ionized gas for the case of a gas jet impinging on water, based on shadowgraph experiments and computational two-phase fluid and plasma modelling. We focus on the interfacial dynamics relevant to electrohydrodynamic (EHD) gas flow, so-called electric wind, which is induced by the momentum transfer from accelerated charged particles to neutral gas under an electric field. A weakly ionized gas jet consisting of periodic pulsed ionization waves5, called plasma bullets, exerts more force via electrohydrodynamic flow on the water surface than a neutral gas jet alone, resulting in cavity expansion without destabilization. Furthermore, both the bidirectional electrohydrodynamic gas flow and electric field parallel to the gas – water interface produced by plasma interacting ‘in the cavity’ render the surface more stable.

摘要翻译：撞击气体射流会导致液体表面凹陷，任何观察过通过吸管吹气而产生空腔的人都很熟悉这种现象。作者基于阴影图实验和计算两相流体和等离子体模型，论证了在气体射流撞击水的情况下，弱电离气体对这种不稳定性的稳定作用。他们重点研究了与电流体动力（EHD）气体流动相关的界面动力学，即所谓的电风，它是在电场下由加速带电粒子向中性气体的动量转移所引起的。由周期性脉冲电离波组成的弱电离气体射流被称为等离子体子弹，它通过电流体动力流对水面施加的力比单独的中性气体射流更大，导致空腔膨胀而不产生不稳定。此外，“腔内”等离子体相互作用产生的双向电流体动力气体流和平行于气-水界面的电场使表面更加稳定。

文中插图：

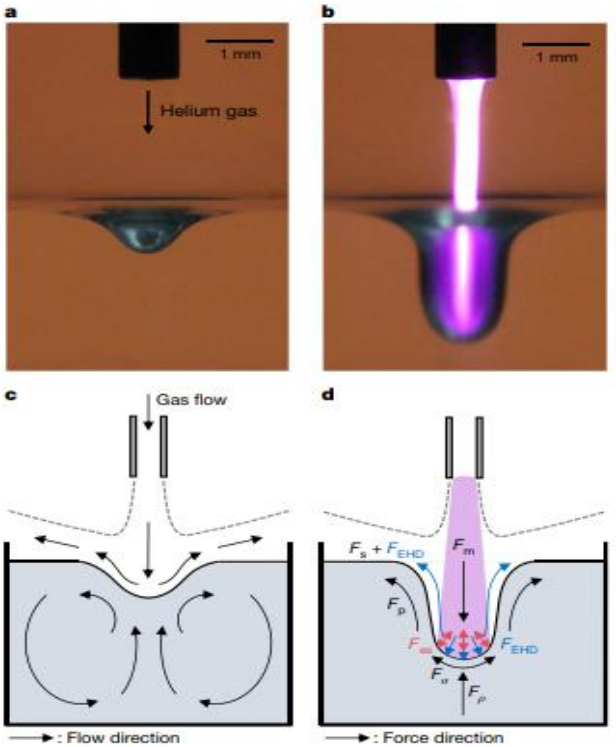

Fig. 1 | Cavity formation at water surfaces subjected to jet forces. **a**, **b**, Shadowgraph images presenting the depression of a free surface of distilled water by a neutral helium gas jet (**a**) and a weakly ionized helium gas jet (**b**) at a 0.90-slpm gas flow rate (slpm, standard litres per minute). The plasma jet was operated by a 3.0-kV positive pulse with a 50% duty cycle and a 10-kHz repetition frequency. Note that a plasma emission discontinuity is caused by the large water surface curvature. Notably, the plasma-forced cavity shape in **b** rapidly returns to the initial shape in **a** when the plasma jet is turned off

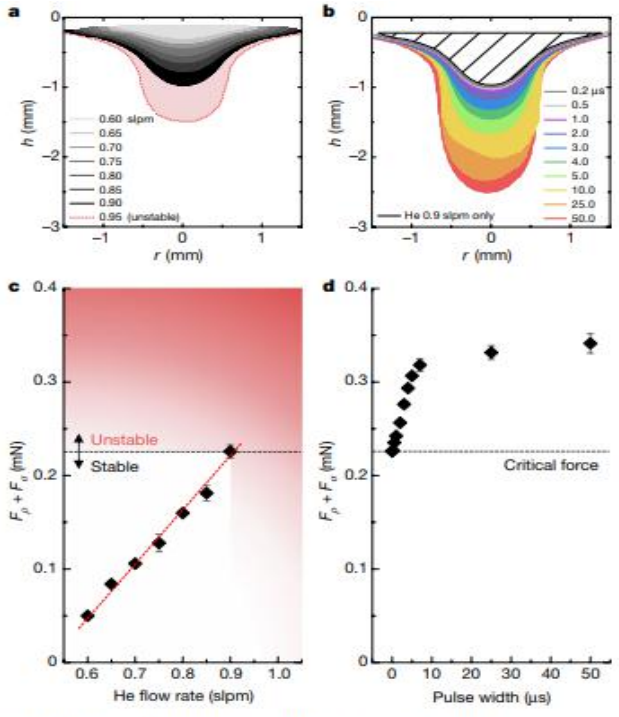

Fig. 2 | Deformed water surfaces and the corresponding force. a, Comparison of the water surface profiles at different flow rates of the helium gas jet extracted from shadowgraph images (Extended Data Fig. 2a). Greyscale shaded areas depict stable cavities. The cavities became unstable beyond a 0.90-slpm flow rate, as highlighted in red. **b**, Cavity deformation caused by 10-kHz pulsed plasma jets with 0.2–50.0-μs pulse widths (duration), extracted from Extended Data Fig. 2b. The flow rate of neutral helium gas remained constant at 0.90 slpm, and the pulse height was set at 3.0 kV. The area with black diagonal lines indicates the region of stable cavity for He at 0.90 slpm.

[3]Multistable inflatable origami structures at the metre scale

米级多稳定充气折纸结构

出版信息：Nature volume 592, pages 545 – 550 (2021)

作者：J. A. Paulson School of Engineering and Applied Sciences, Harvard University, Cambridge, MA, USA

第一作者单位：Clarendon Laboratory, Department of Physics, University of Oxford, Oxford, UK

全文链接：https://www.nature.com/articles/s41586-021-03407-4

Abstract：From stadium covers to solar sails, we rely on deployability for the design of large-scale structures that can quickly compress to a fraction of their size. Here we draw inspiration from origami to design rigid-walled deployable structures that are multistable and inflatable. Guided by geometric analyses and experiments, we create a library of bistable origami shapes that can be deployed through a single fluidic pressure input. We then combine these units to build functional structures at the metre scale, such as arches and emergency shelters, providing a direct route for building large-scale inflatable systems that lock in place after deployment and offer a robust enclosure through their stiff faces.

摘要翻译：从体育场罩到太阳帆，人们依靠可展开性来设计大型结构，这些结构可以迅速压缩到其体积的一小部分。作者从折纸艺术中汲取灵感，设计了多稳定、可膨胀的刚性壁可展开结构。在几何分析和实验的指导下，他们创建了一个双稳态折纸形状库，可以通过一个单一的流体压力输入部署。然后，他们将这些单元结合起来，在米尺度上构建功能结构，如拱门和应急避难所，为建造大型充气系统提供了直接的路径，这些系统在部署后可以锁定，并通过它们僵硬的表面提供一个坚固的外壳。

文中插图：

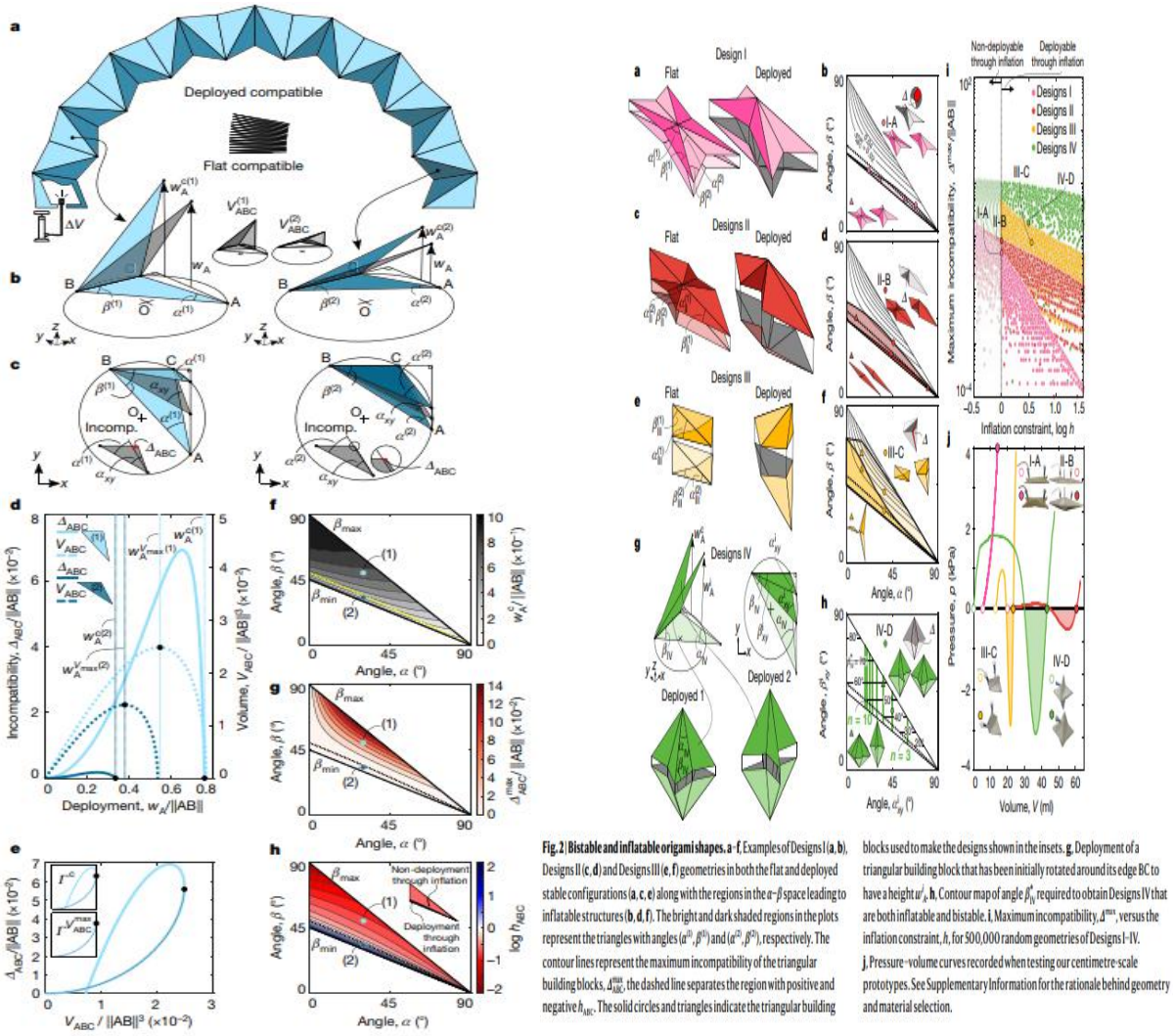

Fig. 2 | Bistable and inflatable origami shapes. a–**f**, Examples of Designs I (**a**, **b**), Designs II (**c**, **d**) and Designs III (**e**, **f**) geometries in both the flat and deployed stable configurations (**a**, **c**, **e**) along with the regions in the α–β space leading to inflatable structures (**b**, **d**, **f**). The bright and dark shaded regions in the plots represent the triangles with angles ($\alpha^{(1)}$, $\beta^{(1)}$) and ($\alpha^{(2)}$, $\beta^{(2)}$), respectively. The contour lines represent the maximum incompatibility of the triangular building blocks. Δ^{max}_{ABC}, the dashed line separates the region with positive and negative h_{ABC}. The solid circles and triangles indicate the triangular building blocks used to make the designs shown in the insets. **g**, Deployment of a triangular building block that has been initially rotated around its edge BC to have a height w'_A. **h**, Contour map of angle β^*_{IV} required to obtain Designs IV that are both inflatable and bistable. **i**, Maximum incompatibility, Δ^{max}, versus the inflation constraint, h, for 500,000 random geometries of Designs I–IV. **j**, Pressure–volume curves recorded when testing our centimetre-scale prototypes. See Supplementary Information for the rationale behind geometry and material selection.

[4]Non-reciprocal phase transitions

非互易相变

出版信息：Nature volume 592, pages 363 – 369 (2021)

作者：Michel Fruchart, Ryo Hanai, Peter B. Littlewood & Vincenzo Vitelli

第一作者单位：James Franck Institute and Department of Physics, University of Chicago, Chicago, IL, USA

全文链接：https://www.nature.com/articles/s41586-021-03375-9

Abstract： Out of equilibrium, a lack of reciprocity is the rule rather than the exception. Although wave propagation in non-reciprocal media has recently been closely studied, less is known about the consequences of non-reciprocity on the collective behaviour of many-body systems. Here we show that non-reciprocity leads to time-dependent phases in which spontaneously broken continuous symmetries are dynamically restored. We illustrate this mechanism with simple robotic demonstrations. The resulting phase transitions are controlled by spectral singularities called exceptional points. We describe the emergence of these phases using insights from bifurcation theory and non-Hermitian quantum mechanics. Our approach captures non-reciprocal generalizations of three archetypal classes of self-organization out of equilibrium: synchronization, flocking and pattern formation. Collective phenomena in these systems range from active time-(quasi) crystals to exceptional-point-enforced pattern formation and hysteresis. Our work lays the foundation for a general theory of critical phenomena in systems whose dynamics is not governed by an optimization principle.

摘要翻译：失去平衡，缺乏互易是普遍现象，而不是例外。虽然近期人们对非互易介质中波的传播进行了深入研究，但对于非互易性对多体系统群集行为的影响却知之甚少。研究组证明非互易性导致了时变相，在这些相位中自发破坏的连续对称性被动态恢复。他们用简单的机器人演示来说明这个机制。由此产生的相变被称为异常点的光谱奇点控制。研究组用分岔理论和非厄米量子力学的观点来描述这些相的出现。该方法捕捉到了失去平衡的三类自组织原型的非互易推广：同步、群集和模式形成。这些系统中的集体现象范围从活跃的时间（准）晶体到异常点强制模式形成和滞后不等。该研究工作为系统临界现象的一般理论奠定了基础，该系统的动力学不受优化原则的支配。

文中插图：

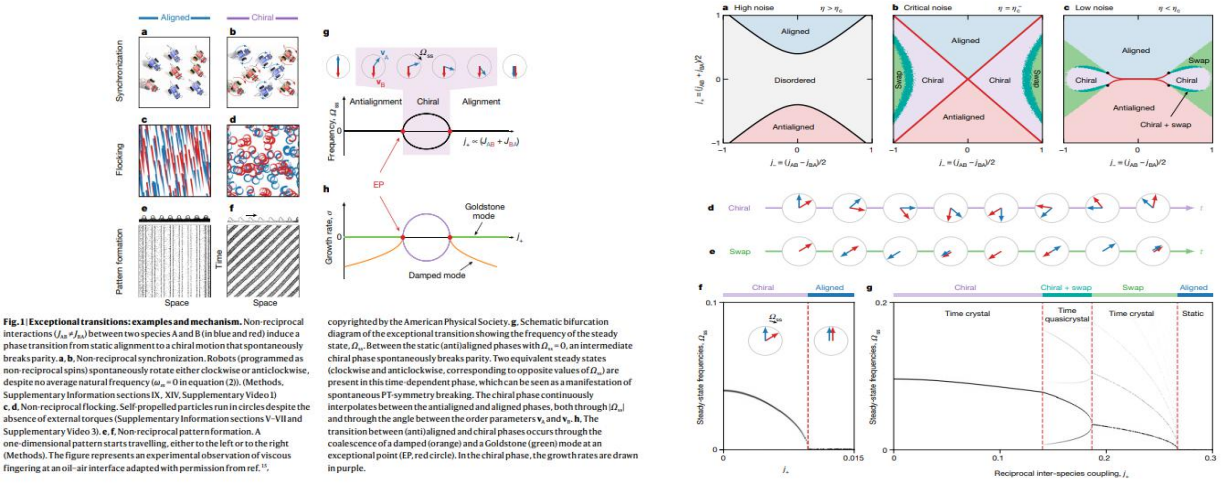

Fig. 1 | Exceptional transitions: examples and mechanism. Non-reciprocal interactions ($J_{AB} \neq J_{BA}$) between two species A and B (in blue and red) induce a phase transition from static alignment to a chiral motion that spontaneously breaks parity. **a**, **b**, Non-reciprocal synchronization. Robots (programmed as non-reciprocal spins) spontaneously rotate either clockwise or anticlockwise, despite no average natural frequency ($\omega_{av} = 0$ in equation (2)). (Methods, Supplementary Information sections IX, XIV, Supplementary Video 1) **c**, **d**, Non-reciprocal flocking. Self-propelled particles run in circles despite the absence of external torques (Supplementary Information sections V–VII and Supplementary Video 3). **e**, **f**, Non-reciprocal pattern formation. A one-dimensional pattern starts travelling, either to the left or to the right (Methods). The figure represents an experimental observation of viscous fingering at an oil–air interface adapted with permission from ref. [15], copyrighted by the American Physical Society. **g**, Schematic bifurcation diagram of the exceptional transition showing the frequency of the steady state, Ω_{ss}. Between the static (anti)aligned phases with $\Omega_{ss} = 0$, an intermediate chiral phase spontaneously breaks parity. Two equivalent steady states (clockwise and anticlockwise, corresponding to opposite values of Ω_{ss}) are present in this time-dependent phase, which can be seen as a manifestation of spontaneous PT-symmetry breaking. The chiral phase continuously interpolates between the antialigned and aligned phases, both through $|\Omega_{ss}|$ and through the angle between the order parameters $\mathbf{v}_A$ and $\mathbf{v}_B$. **h**, The transition between (anti)aligned and chiral phases occurs through the coalescence of a damped (orange) and a Goldstone (green) mode at an exceptional point (EP, red circle). In the chiral phase, the growth rates are drawn in purple.

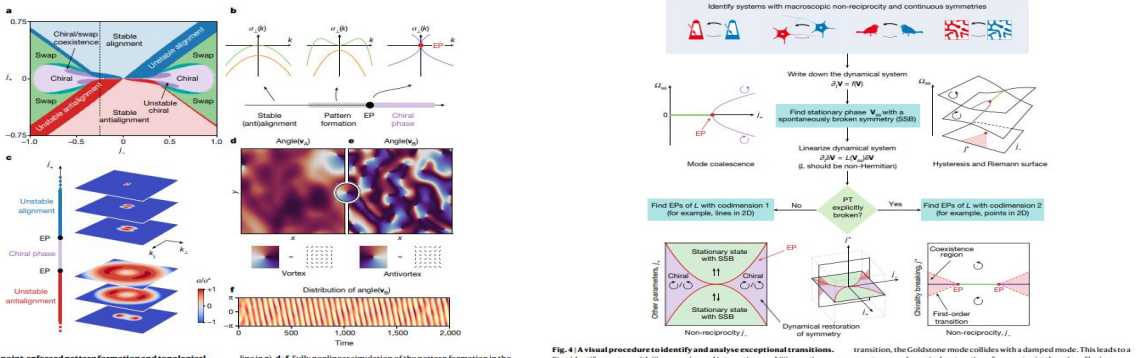

Fig. 3 | Exceptional-point-enforced pattern formation and topological defects. Convective terms and exceptional points (EPs) give rise to pattern formation near the transition lines. **a**, Numerical phase diagram including the linear stability analysis of the (anti)aligned and chiral phases in the non-reciprocal Toner–Tu model (the stability of the swap and chiral+swap phases is not analysed). Units are arbitrary. **b**, The coalescence of the Goldstone mode with a damped mode leads to instabilities at finite momentum. The growth rate of transverse perturbations $\sigma_\perp(k)$ becomes positive, and has a maximum σ^* at a finite wavevector k^*. **c**, Normalized growth rate $\sigma(k)/\sigma^*$ as a function of wavevector, for different values of $J_\times$ at fixed $J_\parallel$ (along the dashed line in **a**). **d**–**f**, Fully nonlinear simulation of the pattern formation in the unstable aligned regime. In **d**, **e**, we show snapshots of the angle of the order parameters $\mathbf{v}_A$ and $\mathbf{v}_B$ with a fixed direction (Supplementary Video 4). Numerous topological defects (vortices and antivortices) are present. In **f**, we show the time evolution (arbitrary units) of the histogram of the angle between $\mathbf{v}_A$ and a fixed direction ($\mathbf{v}_B$ has identical features). Parameters are the same as in Fig. 2 with $\eta/\eta_c = 0.5$. We set $\sigma_0^2 = 0.06$ and $\sigma_0^2 = 0.01$. Simulations in **d**–**f** are performed on a $2L \times 2L$ box with periodic boundary conditions, and $L = 0.32$, $J_\times = 0.1$, $J_\parallel = 0.2$ (see Methods).

Fig. 4 | A visual procedure to identify and analyse exceptional transitions. First identify a system with (i) non-reciprocal interactions and (ii) a continuous symmetry. Write down the dynamical system for the order parameter(s) $\mathbf{V}$. Find a time-independent steady state $\mathbf{V}_{ss}$ with spontaneously broken continuous symmetry (SSB, green regions). Linearize around the time-independent steady state. The linear operator (Jacobian matrix) $L(\mathbf{V})$ has a vanishing eigenvalue (Goldstone mode). Exceptional points (EP; red points and continuous red lines) of $L(\mathbf{V})$ with zero eigenvalue mark the transition. We distinguish (I) parameters J that do not explicitly break parity and (II) parameters J^* that do. We further split the parameters J into (1) parameters $J_\parallel$ encoding the non-reciprocity and (2) other parameters $J_\times$. When $J^* = 0$ (left panel), the exceptional points have codimension 1 (lines in a two-dimensional parameter space). At the exceptional transition, the Goldstone mode collides with a damped mode. This leads to a spontaneous dynamical restoration of symmetry (at the price of losing time-translation invariance). In the chiral phase (purple), the space of equivalent steady states (corresponding to the broken symmetry) is travelled in a direction chosen at random (clockwise or anticlockwise). When $J^* \neq 0$, this mechanism competes with an explicit rotation of the order parameter. This leads to extended regions (light red) starting at the exceptional point, now of codimension 2) in which the (anti)clockwise states coexist, marked by first-order transitions and hysteresis: the complex frequency has a Riemann surface (Extended Data Fig. 5). Both cases are organized in three-dimensional phase diagram (bottom, middle panel).

[5]Subterahertz collective dynamics of polar vortices

极涡的亚赫兹群集动力学

出版信息：Nature volume 592, pages 376 – 380 (2021)

作者：Qian Li, Vladimir A. Stoica, Marek Paściak, Yi Zhu, Yakun Yuan, Tiannan Yang, et al.

第一作者单位：Advanced Photon Source, Argonne National Laboratory, Lemont, IL, USA

School of Materials Science and Engineering, Tsinghua University, Beijing, China

国内相关报道：http://www.mse.tsinghua.edu.cn/info/1062/1881.htm

全文链接：https://www.nature.com/articles/s41586-021-03342-4

Abstract：The collective dynamics of topological structures are of interest from both fundamental and applied perspectives. Topological structures constructed from electrical polarization, rather than electron spin, have recently been realized in ferroelectric superlattices, and these are promising for ultrafast electric-field control of topological orders. However, little is known about the dynamics underlying the functionality of such complex extended nanostructures. Here, using terahertz-field excitation and femtosecond X-ray diffraction measurements, we observe ultrafast collective polarization dynamics that are unique to polar vortices, with orders-of-magnitude higher frequencies and smaller lateral size than those of experimentally realized magnetic vortices. A previously unseen tunable mode, hereafter referred to as a vortexon, emerges in the form of transient arrays of nanoscale circular patterns of atomic displacements, which reverse their vorticity on picosecond timescales. Its frequency is considerably reduced at a critical strain, indicating a condensation of structural dynamics. We use first-principles-based atomistic calculations and phase-field modelling to reveal the microscopic atomic arrangements and corroborate the frequencies of the vortex modes. The discovery of subterahertz collective dynamics in polar vortices opens opportunities for electric-field-driven data processing in topological structures with ultrahigh speed and density.

摘要翻译：拓扑结构的群集动力学在基础和应用两个方面都很有意义。最近在铁电超晶格中已经实现了由电极化而非电子自旋构成的拓扑结构，这对拓扑序的超快电场控制而言前景广阔。然而，人们对这种复杂的扩展纳米结构功能的动力学机制知之甚少。研究组利用太赫兹场激发和飞秒 X 射线衍射测量，观察到极涡特有的超快群集极化动力学，其频率比实验实现的磁涡高几个数量级，横向尺寸更小。一种以前未发现的可调谐模式（下文称为涡旋）以纳米尺度原子位移圆形模式的瞬态阵列形式出现，可在皮秒时间尺度上逆转其涡度。其频率在临界应变下显著降低，表明结构动力学的凝结。研究组使用基于第一性原理的原子计算和相场模型来揭示微观原子排列并证实涡旋模式的频率。极涡中亚赫兹群集动力学的发现为超高速高密度拓扑结构中电场驱动的数据处理提供了机会。

文中插图：

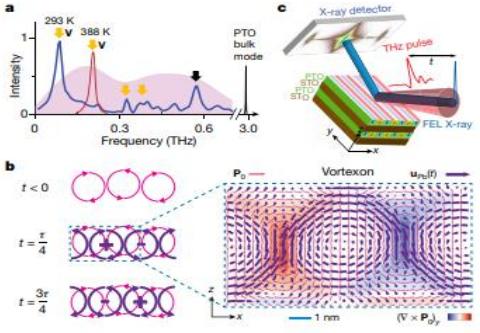

Fig. 1 | Emergence of the collective dynamics of polar vortices and its experimental detection. a, Fourier spectra (blue) of calculated time-dependent response of polar vortices on THz-field excitation. The spectrum of the THz pulse is shown as a broad pink background. The collective modes of polar vortices (orange arrows) are shown as a separate set of modes with respect to the known superlattice acoustic modes (black arrow) and the soft mode of $PbTiO_3$ at room temperature. The vortexon mode (V) shifts to higher frequency (red peak; note that this is not the calculated peak but a schematic peak to show the temperature dependence) as sample temperature increases. **b**, Emergence and evolution of the vortexon (atomic displacement vortices, purple circles) during its oscillation period τ, overlaid with the static polarization vortices (magenta circles). + and −, the signs of vortexon vorticity, which reverse dynamically. Right, zoomed-in view of the region of the dashed box with the calculated static polarization (magenta arrows) and lead-cation displacement (purple arrows) in each unit cell of the vortexon mode at $t = \tau/4$. **c**, Schematic of THz-pump and X-ray-diffraction-probe experiment using an X-ray free-electron laser (FEL). The coloured stripes on the $(PbTiO_3)_{16}/(SrTiO_3)_{16}$ (PTO/STO) superlattice film represent in-plane vortex orders with opposite polarization vorticity.

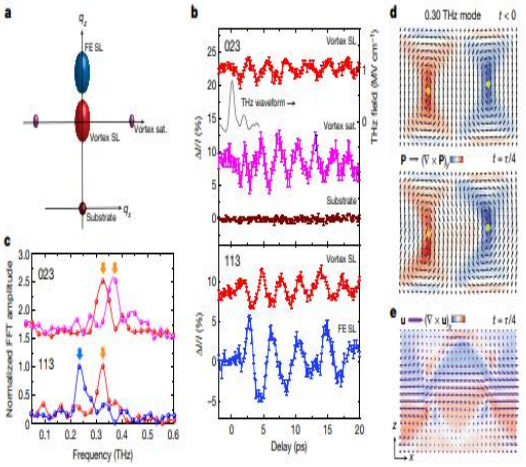

Fig. 2 | High-frequency collective modes. a, Schematic of the probed Bragg peaks in the q_z–q_x plane of the reciprocal space around the 023, 113 and 004 substrate peaks. FE, ferroelectric a_1/a_2 structure; sat., satellite peak; SL, superlattice peak; substrate, DSO peak. **b**, Normalized change of diffraction intensity of the Bragg peaks (indicated by the same colour scheme as in **a**) as a function of delay, with the measured THz excitation pulse overlaid (THz waveform scale indicated on the right). The error bars show the standard errors. **c**, The corresponding Fourier spectra with marked vortex modes (orange arrows) and FE modes (blue arrow). The curves in **b** and **c** are offset vertically for clarity. FFT, fast Fourier transform. **d**, Polarization (**P**) of a calculated 0.30-THz vortex mode at the equilibrium state ($t < 0$) and the sinusoidal maximum ($t = \tau/4$), with associated vorticity (colour). **e**, Lead-cation displacements (**u**) and associated vorticity (colour) at $t = \tau/4$. The structural distortion is enhanced for better visibility.